

# Identification of mechanisms of magnetic transitions using an efficient method for converging on first order saddle points

Moritz Sallermann,<sup>1,2,3,\*</sup> Hendrik Schrautzer,<sup>1,†</sup> Pavel F. Bessarab,<sup>1,4,‡</sup> and Hannes Jónsson<sup>1,§</sup>

<sup>1</sup>*Science Institute and Faculty of Physical Sciences, University of Iceland, VR-III, 107 Reykjavík, Iceland*

<sup>2</sup>*Peter Grünberg Institut and Institute for Advanced Simulation, Forschungszentrum Jülich and JARA, 52425 Jülich, Germany*

<sup>3</sup>*Department of Physics, RWTH Aachen University, 52056 Aachen, Germany*

<sup>4</sup>*Department of Physics and Electrical Engineering, Linnaeus University, SE-39231 Kalmar, Sweden*

(Dated: March 19, 2024)

A method for locating first order saddle points on the energy surface of magnetic systems is described and several applications presented where the mechanism of various magnetic transitions is identified. The starting point of the iterative algorithm involved in the method can be anywhere, even close to a local energy minimum representing an initial state of a magnetic system and, in contrast to chain-of-states methods, the final state need not be specified. Convergence on the saddle points is guided by a negative energy gradient whose component along the minimum mode of the system is inverted, effectively transforming the neighbourhood of the saddle point to that of a local minimum. The method requires only the lowest two eigenvalues and corresponding eigenvectors of the Hessian of the system's energy and they are found using a quasi-Newton limited-memory Broyden–Fletcher–Goldfarb–Shanno solver for the minimization of the Rayleigh quotient without evaluation of the Hessian itself. The efficient implementation of the method and its linear scaling with the system size make it applicable to large systems. Applications are presented to transitions in systems that reveal significant complexity of co-existing magnetic states, such as skyrmions, skyrmion bags, skyrmion tubes, chiral bobbars and globules. When combined with harmonic rate theories, the presented method can be used for simulations of the long time-scale dynamics of complex magnetic systems characterized by multiple metastable states.

## I. INTRODUCTION

The task of identifying the mechanism of possible transitions and estimating the corresponding rates within either the harmonic transition state theory (HTST) [1, 2] or Kramers/Langer theory [3, 4] involves finding low-lying first order saddle points (SPs) on the energy surface, adjacent to the initial state minimum. A first-order SP is an extremal point, i.e. the gradient is zero, and one and only one eigenvalue of the Hessian matrix is negative. A simulation of long timescale dynamics, using the adaptive kinetic Monte Carlo algorithm [5, 6], necessitates the determination of the rate of various possible transitions, without any prior assumptions about the mechanism or final state. This approach can also be used as the basis for the global optimization of an objective function in a broader context [7], as well as for path optimization [8], e.g. in calculations of tunneling within instanton theory [9] and radio wave propagation [10].

The development of methods for finding first order SPs on high-dimensional energy surfaces has, primarily, been in the context of atomic rearrangements, such as diffusion and chemical reactions [11]. Analogous methods can be used to study magnetic transitions [12, 13] where magnetic moments rotate, for example, in the collapse of localized magnetic structures [14]. However, the

curvature of the configuration space of magnetic systems poses additional challenges. The central objective of such methods is the search for a first-order SP, preferably starting near a local energy minimum representing an initial state of the system. The task can be split into two distinct phases: Firstly, the system is slightly perturbed, away from the energy minimum and a climb up the energy surface carried out until at least one eigenvalue of the Hessian matrix turns negative [5, 7]. This is referred to as the escape phase. Secondly, each component of the torque is reflected at the plane defined by the direction of the eigenvector  $v_1$  and the magnetic moment. We refer to this as torque reflection using the **minimum mode** (TRUMM). This reflection essentially transforms the problem of finding a first order SP into a minimization, a much simpler optimization task.

A straightforward implementation of this method would involve the evaluation of the Hessian and a solution of the full eigenvalue problem. However, the computational effort involved in solving the eigenvalue problem increases rapidly with system size. The number of spins in relevant model systems can be large, often on the order of  $10^5$  to  $10^7$ . Henceforth, even the mere evaluation of the full Hessian can require substantial effort. In particular, the explicit inclusion of long-range magnetostatic effects, as is frequently necessary in large three-dimensional systems, can be computationally infeasible in such an approach. The reason is that the Hessian matrix then becomes dense and storing it can exceed the working memory capacity of a typical compute node, even for systems of moderate size. In addition, models that go beyond a simple Heisenberg approach like, for

\* [moritz.sallermann@rwth-aachen.de](mailto:moritz.sallermann@rwth-aachen.de)

† [hes93@hi.is](mailto:hes93@hi.is)

‡ [pavel.bessarab@lnu.se](mailto:pavel.bessarab@lnu.se)

§ [hj@hi.is](mailto:hj@hi.is)

example, the non-collinear extension of the Alexander-Anderson model [15], make the computation of second order derivatives a significant task.

Since the TRUMM method only requires the eigenvectors corresponding to the two lowest eigenvalues of the Hessian – the lowest one for the reflection, and the next one to ensure that a first order SP has been reached – the solution of the full eigenvalue problem is, in fact, not needed. A more efficient implementation of TRUMM is, therefore, possible and is described in detail in this article.

When the final state of a magnetic transition is specified, in addition to the initial state, the minimum energy path (MEP) between the corresponding minima on the energy surface can be found using the geodesic nudged elastic band (GNEB) method [14]. Since a first order SP is represented by the point of highest energy along the MEP, an accurate estimate of it can be obtained from the climbing image variant of the method. A more efficient approach to thoroughly converge on the SP, however, is to converge the GNEB with a rather large tolerance and, subsequently, to apply TRUMM with the highest energy GNEB image as input. This saves computational effort, analogous to what has become a routine procedure in calculations of rates for particle rearrangements [16].

Previous implementations of TRUMM, for magnetic systems, have been rather preliminary in several respects and have only been described briefly. They have, nonetheless, been used successfully in identifying, for example, duplication transitions of magnetic skyrmions [17, 18], as well as SPs, representing complex annealing mechanisms of three-dimensional hopfions [19].

In the present article, we describe an efficient way of computing the modified torque in the TRUMM method, using an iterative method that does not require the evaluation of the Hessian. It is, thereby, applicable to large systems and more complex Hamiltonians than the Heisenberg form. It is novel in that the lowest two eigenvalues and corresponding eigenvectors are found simultaneously, using the generalized Rayleigh quotient, and an L-BFGS optimizer on the Grassmann manifold. The method is described in detail in Sec. II. We also include a subsection on an implementation of the escape phase that proved to sample the various SPs, which were encountered in the analyzed systems, sufficiently well.

This is followed by Sec. III, where the various application systems are described. Results of several TRUMM calculations are presented Sec. IV and, further, the performance is compared to that of a partial eigenvalue calculation with the Intel MKL library. Among our findings is a mechanism that has not been identified previously, involving the conversion of a skyrmion to a skyrmion bag, also called skyrmionium. In the final section, Sec. V, we present conclusions. Appendices A-C give further detail on the present implementation of the TRUMM method and the method used here for the escape phase.

## II. METHOD

An iterative optimization procedure involved in the TRUMM method starts in the vicinity of some local energy minimum of a magnetic system and follows two stages: i) Escape from the convex region near the minimum; ii) Convergence on the first order SP of the energy surface. This two-stage procedure is to be repeated multiple times so as to identify, with a high degree of certainty, all relevant SPs surrounding the given energy minimum. Convergence on various SPs is achieved by generating several different starting points near the energy minimum and by following different scenarios in the escape stage. For example, the convex region can be escaped by displacing the system along the energy gradient, or by following various eigenmodes of the system [17]. In studies of atomic rearrangements, a method of sampling of a hypersphere around the energy minimum has been developed [7, 20, 21]. Clearly, the choice of the escape strategy affects the efficiency of the method in finding as many distinct SPs as possible while keeping the number of the TRUMM runs to a minimum. Choosing the optimal escape strategy is an important problem, which, however, goes beyond the scope of the present study, and here we focus on the efficient implementation of the second stage of the SP search – the SP convergence stage. Nevertheless, the escape methods used to obtain the results of this study are described in Appendix C for completeness.

At a certain iteration of the escape stage, the minimum eigenvalue of the Hessian of the system's energy as a function of the orientation of the magnetic moments turns negative, which is an indication that the region near an SP has been reached and that the SP convergence stage of the TRUMM method needs to be started. In contrast to the escape stage, the strategy for advancing the system during the convergence stage is defined unambiguously. It is guided by a magnetic torque designed so as to carry out a maximization of the energy along the direction of the minimum mode, i.e. the eigenvector of the Hessian corresponding to the minimal eigenvalue, and minimization along all other directions. Such formulation eventually results in a convergence on a first-order SP rather than a minimum. Specifically, the torque on the  $i$ th magnetic moment in the system is defined as follows:

$$\vec{T}_i = \vec{s}_i \times \vec{B}_i, \quad (1)$$

where  $\vec{s}_i$  is the unit vector in the direction of  $i$ th magnetic moment, and  $\vec{B}_i$  is the effective field whose component along the minimum mode is inverted:

$$\vec{B}_i = -\vec{\nabla}_i E + 2(\nabla E \cdot \vec{Q})\vec{Q}_i. \quad (2)$$

Here,  $E$  is the energy of the system of  $N$  interacting magnetic moments,  $\vec{Q} = (\vec{Q}_1, \vec{Q}_2, \dots, \vec{Q}_N)$  is the unit vector representing the minimum mode, and  $\nabla = (\vec{\nabla}_1, \vec{\nabla}_2, \dots, \vec{\nabla}_N)$ , with  $\vec{\nabla}_i \equiv \partial/\partial\vec{s}_i$ . The minimum

mode is the eigenvector corresponding to the lowest eigenvalue  $\mathbf{Q} = \mathbf{v}_1$ . Everywhere in this article, unless stated otherwise, symbols with an arrow above denote 3-dimensional vectors, whereas bold symbols denote  $2N$  or  $3N$ -dimensional vectors. Furthermore we use the indices  $i, j$  for indexing the spins while Greek letters indicate the index of the eigenmodes. The reflection along the minimum mode makes the effective field correspond to the neighbourhood of a minimum of  $E(\mathbf{s})$  rather than that of an SP, which reflects the basic idea of the method to transform the problem of locating first-order SPs into a much simpler task of the gradient-based minimization.

Depending on particular application, it might be more convenient, but equivalent, to consider the transverse component of the effective field as a guiding vector in the SP convergence stage instead of the torque:

$$\vec{F}_i = \vec{B}_i - (\vec{B}_i \cdot \vec{s}_i) \vec{s}_i, \quad (3)$$

which can be referred to as magnetic force.

Once the modified torque [see Eq. (1)] or force [see Eq. (3)] has been computed, the spin orientations need to be propagated in a direction dependent on (but not necessarily equal to) the modified force. The dependency of the propagation direction on the (history of) modified force(s) is a detail of the numerical optimization routine. For example, a steepest descent minimization will give different propagation directions from a conjugate gradient solver. While in principle many different optimization routines can be used, we employ another L-BFGS solver to propagate the spin directions according to the modified force. This results in two nested L-BFGS solvers, (i) an outer solver for the spin propagation and (ii) an inner solver for the computation of the eigenmodes (see B). In Sec. IV A the above described methodology is compared with an implementation of the TRUMM method, which uses a state of the art extremal eigensolver based on a Krylov Schur [22] method implemented in the Intel MKL library (TRUMM/KS).

One important aspect of applying the algorithm to magnetic systems is the correct consideration of the configuration space  $\mathcal{R}$ , which is a Riemannian manifold due to constraints on the length of the magnetic moments: Typically, the magnitude of the magnetic vectors is either assumed to be constant irrespective of the orientation, or it is treated as a fast variable within the adiabatic approximation, i.e. calculated for fixed values of the orientation treated as a slow variable [15]. When modelling a system with  $N$  magnetic moments, the resulting configuration space is, therefore, a direct product of  $N$  two-dimensional spheres  $S_2$  associated with each magnetic moment vector:

$$\mathcal{R} = \bigotimes_N S_2 \subset \mathbb{R}^{3N}, \quad (4)$$

giving rise to  $n = 2N$  degrees of freedom. It is computationally advantageous to work in the embedding space  $\mathbb{R}^{3N}$  and to eliminate the  $N$  superfluous degrees of freedom by applying the projection operator approach [23].

## A. Evaluation of the Hessian matrix

For the TRUMM algorithm it is of great importance to perform a geometrically correct calculation of the Hessian matrix  $H$ , which takes the connection between disparate tangent spaces into account. How to perform such a calculation and find the corresponding eigenmodes, within the projector approach, is described in Ref. [17] and also Ref. [24]. It shall be briefly introduced here.

The Hessian  $H^{3N} \in \mathbb{R}^{3N \times 3N}$  in the  $3N$ -dimensional embedding Euclidean space is given by the second order derivatives of Eq. (15) with respect to the cartesian spin-components. The constraint to the  $2N$  physical degrees of freedom is achieved in two steps. First, the shape operator  $\mathcal{L}$  is subtracted from  $H^{3N}$ . The shape operator is a diagonal matrix of the following form

$$\mathcal{L} = \begin{pmatrix} B_1 & \dots & 0 \\ \vdots & \ddots & \vdots \\ 0 & \dots & B_N \end{pmatrix} \in \mathbb{R}^{3N \times 3N}, \quad (5)$$

with

$$B_i = \begin{pmatrix} \vec{s}_i \cdot \vec{g}_i & 0 & 0 \\ 0 & \vec{s}_i \cdot \vec{g}_i & 0 \\ 0 & 0 & \vec{s}_i \cdot \vec{g}_i \end{pmatrix} \in \mathbb{R}^{3 \times 3}, \quad (6)$$

where  $\vec{g}_i = \vec{\nabla}_i E$  is the gradient of the energy with respect to the direction of the  $i$ -th spin  $\vec{s}_i$ .

Then, an operator  $U \in \mathbb{R}^{3N \times 2N}$  is applied, that projects embedding space vectors into the tangent space of the current configuration  $\mathbf{s} \in \mathcal{R}$  (see Ref. [17, 24]). Summarily, we compute the Hessian matrix  $H \in \mathbb{R}^{2N \times 2N}$  as

$$H = U^T (H^{3N} - \mathcal{L}) U. \quad (7)$$

Assuming the eigenpairs are denoted as  $(\lambda_\alpha, \mathbf{v}_\alpha)$  with  $\mathbf{v}_\alpha \in \mathbb{R}^{2N}$ , the eigenvectors can be projected back into the embedding space, if needed, by applying the projection operator:

$$\mathbf{v}_\alpha^{3N} = U \mathbf{v}_\alpha. \quad (8)$$

## B. Finding the lowest modes

For many applications in atomistic spin systems, the calculation of the Hessian matrix with (7) is feasible when a sparse matrix format is used. The main exceptions are dense large Hessians, which can arise in simulations with explicit dipole-dipole interactions. The evaluation of the Hessian eigenmodes with minimal eigenvalues tends to be a computational bottleneck, which will be addressed in the following.

While they are technically not needed for the evaluation of the modified force, it is useful to know the two lowest modes. The reason is that it allows for the identification of mode crossings as well as the determination

of regions in the vicinity of a first order SP, where the eigenvalue of the lowest mode is negative and of the second lowest mode at least zero. In the interest of reducing the computational effort, it is advisable to only compute a partial eigenspectrum of the Hessian matrix and ideally only the two required modes with minimal eigenvalues. Due to the large size of the Hessian matrices encountered in atomistic spin systems, this is of critical importance, because, even for a sparse matrix, the eigenvectors are dense and therefore have heavy memory requirements. Popular algorithms to accomplish this task are Lanczos method [25] and extensions thereof, like Davidson's method [26] and even more sophisticated Krylov subspace methods [27]. In the present work, we will take an alternative approach and focus on the direct minimization of the generalized Rayleigh quotient, defined in Eq. (9) below, with a limited memory Broyden-Fletcher-Goldfarb-Shanno (L-BFGS) solver [28]. Different approaches, like the aforementioned algorithms, may ultimately prove to be favourable, although, we do observe that our method seems to be competitive.

The generalized Rayleigh quotient is defined as

$$R_p(X) = \text{tr } X^T H X \quad X \in G_{n,p} \quad (9)$$

where, to ease the notation, we defined  $n = 2N$ ,  $H$  is the Hessian matrix, while  $X$  is an element of the Grassmann manifold  $G_{n,p}$ , which, intuitively speaking, parametrises the set of  $p$ -dimensional linear subspaces of  $\mathbb{R}^n$ . One possible representation of this manifold is the quotient space  $O_n/O_p \times O_{n-p}$ , where  $O_n$  is the  $n \times n$  orthogonal group. Two  $n \times p$  matrices  $X$  and  $X'$  belong to different equivalency classes of  $G_{n,p}$  if, and only if, their columns span different  $p$  dimensional subspaces. In the special case where  $p = 1$  and a representation of the equivalence class is fixed by normalizing  $\mathbf{x}$ , Eq. (9) reduces to the ordinary Rayleigh quotient

$$R(x) = \frac{\mathbf{x}^T H \mathbf{x}}{\mathbf{x}^T \mathbf{x}} \quad \mathbf{x} \in \mathbb{R}^n. \quad (10)$$

It is well known that, if the generalized Rayleigh quotient (9) is minimized such that

$$\min_{X \in G_{n,p}} \text{tr } X^T H X = \text{tr } X_{\min}^T H X_{\min}, \quad (11)$$

the subspace spanned by the columns of  $X_{\min}$  is the invariant subspace belonging to the  $p$  smallest eigenvalues of  $H$ .

In TRUMM calculations, we are interested in the two lowest modes, i.e. we perform the minimization of (9) with  $p = 2$ , using the gradient

$$\nabla R_p(X) = 2 [HX - X(X^T H X)], \quad (12)$$

which results from the projection of the embedding space derivative of (9) onto the Grassmann manifold [23]. Once  $X_{\min}$  is found, the two lowest modes of  $H$  may be extracted by using the Rayleigh-Ritz procedure, i.e by solving the  $2 \times 2$  eigenvalue problem

$$(X_{\min}^T H X_{\min}) \mathbf{v}_\alpha = \lambda_\alpha \mathbf{v}_\alpha \quad \alpha \in \{1, 2\} \quad (13)$$

and using the Ritz vectors

$$\tilde{\mathbf{v}}_\alpha = X_{\min} \mathbf{v}_\alpha, \quad (14)$$

as the modes of  $H$ .

In our algorithm we apply the method, outlined above, to update approximations of the two minimum modes after each application of the modified force (3), which changes the spin directions and, therefore, the Hessian matrix. More specifically, we apply the L-BFGS algorithm to the minimization problem (11), using the solution of the previous step as an initial guess for  $X$ .

### C. Optimization on the Grassmann manifold

Applying the L-BFGS algorithm to the Grassmann manifold requires some adaptations, which address the challenge of navigating through the manifold's varying tangent spaces [23, 29].

The optimization on the manifold is punctuated by the need to traverse between the tangent spaces and the manifold itself. Generally speaking, this bidirectional movement is facilitated by retractions, which provide a smooth pathway from the tangent space back to the manifold. These mappings ensure that each iteration's move, though calculated in the tangent space, is validly represented on the manifold, adhering to its geometric constraints. In our implementation we make use of the exponential map, which is a special kind of retraction following geodesics. On the Grassmann manifold, the action of the exponential map can be found by the compact singular value decomposition of the tangent vector of the geodesic [23]. This step is performed in Alg. 4.

As the algorithm iterates, it accumulates a history of gradients and displacements that inform its approximation of the inverse Hessian matrix. However, the non-linear geometry of the manifold means that these history vectors no longer reside in a single, coherent tangent space. Instead, they are scattered across the manifold, each anchored to the point of their calculation.

It is therefore necessary to transport this scattered history to the tangent space of the current iterate, allowing the algorithm to reference and utilize these vectors cohesively. By transporting the history vectors into a common tangent space, the L-BFGS method maintains the integrity and applicability of its inverse Hessian approximation. Since we displace the iterate along geodesics, we can make use of the parallel transport equations [23], implemented in Alg. 3.

It turns out that only a few iterations of L-BFGS are needed to obtain an estimate of the eigenmodes, which is sufficiently converged to drive the algorithm towards a SP. It can be beneficial to run a different partial diagonalization algorithm, e.g Lanczos, Davidson or a different Krylov-space based method, after a certain number of iterations (around 100). This can be done at negligible amortized cost.



Further, we note that, if the columns of  $X$  are treated separately, only matrix-vector products are needed (similar to other space based methods). This allows the implementation of the action  $HX$  as a finite difference between the energy gradients  $\nabla E$ , which can provide another significant speedup. This is the case especially when dipole-dipole interactions are considered explicitly and, consequently, the Hessian is dense.

We summarize the formulas employed in the finite difference scheme, which contain some minor subtleties due to the spin length constraints, in App. A. App. B provides code listings for the L-BFGS algorithm on the Grassmann manifold.

#### D. Further Considerations

1. *Return to the convex region:* Occasionally, following the modified force (3) can lead *back* into the convex region of a minimum. This can occur, since the modified force only differs from the actual force  $\mathbf{F} = -\nabla E_{\perp}$  by the scalar product of the minimum mode and the Force,  $\mathbf{v}_1 \cdot \mathbf{F}$ . Thus, if the eigenvector corresponding to the minimum mode is nearly orthogonal to the force  $\mathbf{F}$ , the TRUMM optimization is essentially an energy minimization leading back to the convex region.

2. *Minimum energy path:* Once a first-order SP and the corresponding unstable mode have been determined, it is straightforward to generate the MEP. To achieve this, two points near the SP are generated by shifting slightly back and forth along the unstable mode. Then, a minimization is carried out starting with the displaced configurations until the two local energy minima corresponding to the initial and final states associated with this SP are reached. During the minimization, the cumulative geodesic distance can be recorded to provide the MEP, equivalent to the path that would be obtained by the CI-GNEB method if both initial and final state minima were known beforehand.

### III. MODEL

The TRUMM/RQM method described in Sec. II can in principle be applied to all magnetic energy models that depend on the orientation of the spins  $\vec{s}_i$  with constant length. For example, all variations of different interactions within the framework of the extended Heisenberg model. The theoretical description of topological spin textures in these models parameterized in *ab initio* density functional theory calculations has proven itself in the past also in combination with experimental studies [30, 31]. However, especially with respect to variability and coexistence of different spin textures, some of which are very complex, exemplary parameter studies are also of great value [32]. In particular, we use the following Hamiltonian to demonstrate the developed

TABLE I. Parameters for the extended Heisenberg model (Eq. 15) used for the test-systems in the corresponding result sections. The size refers to the number of unit cells in the  $x$ ,  $y$  and  $z$  direction, respectively. The intervals given for the second application define the investigated parameter space.

System	Size	Section	$J$ (meV)	$D$ (meV)	$B$ (T)
Square	$50 \times 50 \times 1$	IV A	1	0.55	3.1
Square	$50 \times 50 \times 1$	IV B	1	[0.2, 0.8]	[2, 5]
Cubic	$30 \times 30 \times 30$	IV C	1	0.45	2.8

TRUMM/RQM method on square (see Secs. IV A, IV B) and cubic lattice (see Sec. IV C) models:

$$H = -J \sum_{i,j} \vec{s}_i \cdot \vec{s}_j - D \sum_{i,j} \hat{d}_{ij} \cdot (\vec{s}_i \times \vec{s}_j) - \mu \sum_i \vec{B}_{\text{ext}} \cdot \vec{s}_i \quad (15)$$

We consider nearest neighbor exchange ( $J$ ) as well as nearest neighbor Bloch-type Dzyaloshinskii-Moriya interaction (DMI) ( $D$ ), which means that the DMI-vector  $\hat{d}_{ij}$  is oriented along the connection line of the interacting spins  $i$  and  $j$ . The magnetic moment is identical for all spins and set to  $\mu = 1 \mu_B$ , where  $\mu_B \approx 0.0579 \text{ meV/T}$  is the Bohr magneton. An external magnetic field  $\vec{B}$  is applied in the  $z$ -direction. This system set-up is similar to the work of Müller *et al.* [17], which is to our knowledge the only publication dealing with the application of TRUMM in magnetic systems. The three dimensional system investigated in Sec. IV C is defined with the parameters of the work of Rybakov *et al.* [33]. For the exact parameters refer to Tab. I.

## IV. RESULTS

### A. Collapse mechanisms of a Skyrmion

In this section we demonstrate the application the TRUMM method to magnetic systems hosting skyrmions, which are among the most intensely studied topological spin textures. We will obtain SPs via the TRUMM method, including minimum energy paths, and reveal specifics of the eigenvalue spectrum encountered, during the runs of the algorithm. Further, we will compare the performance of the Grassmann L-BFGS implementation of the TRUMM method (described in Sec. II B) to an implementation based on Intel's MKL library.

Four distinct collapse mechanisms are investigated

1. the collapse to the ferromagnetic state via radial shrinking, with the corresponding radial symmetric SP  $\text{Sp}_{\text{rad}}$

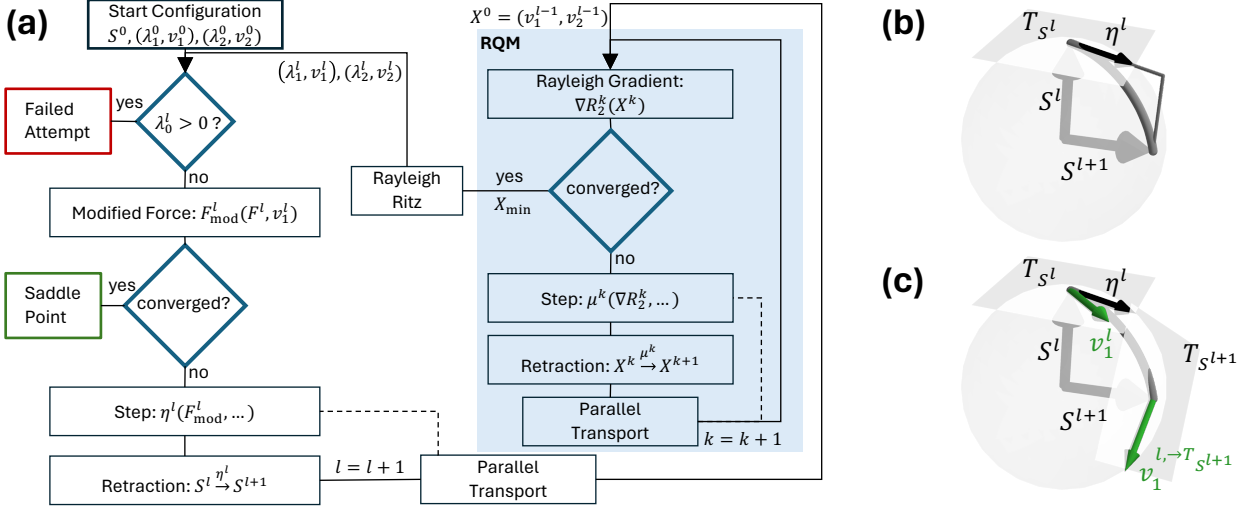


FIG. 1. (a): Flow of the TRUMM/RQM method to emphasize the nesting of the optimization on the spherical spin manifold using the modified force and the optimization on the Grassmannian for updating the eigenmodes. The concepts of Retractions and Parallel Transport are employed for optimization on both manifolds. For a single spin system the concept of the retraction is shown in (b) and the parallel transport of some exemplary eigenvector  $v_1^l$  from iteration  $l$  towards the tangent frame of the spin configuration in iteration  $l + 1$  is shown in (c).

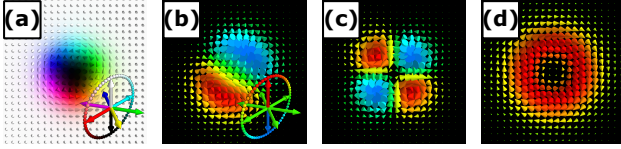


FIG. 2. (a) Skyrmion as a local energy minimum solution of Eq. 15. The inset explains the used conical HSL-colorspace. While the polar angle of the spins is represented by the color angle (hue) the brightness (value) encodes the out-of-plane azimuth angle of the spins for a fixed saturation of 1.0. (b-d) Eigenvectors  $v_\alpha$  of the Hessian  $H$  projected to  $3N$ -dimensional embedding space with indices 1, 3, 5 (from left to right). For the translation modes ( $\alpha = 1, 2$ , (b)) and the fourfold modes ( $\alpha = 3, 4$ ) only one of the two realizations is shown. Part (d) shows the breathing mode ( $\alpha = 5$ ). The colorcode used for the eigenvectors encodes the azimuthal angles of the eigenvector components with a truncated HSV-hue colormap (See inset part (b)).

2. the collapse to the ferromagnetic state via escape through the boundary, with the associated SP  $\text{Sp}_{\text{bound}}$
3. the splitting of a single Skyrmion into two via the so called duplication SP  $\text{Sp}_{\text{dup}}$ , as described in Ref. [17]
4. the transition to the Skyrmion bag, via the SP  $\text{Sp}_{\text{bag}}$

By locally minimizing the energy of a suitable initial configuration, the skyrmion shown in Fig. 2 (a) is obtained. It will be used as a starting configuration for the

SP searches.

The eigenvectors  $v_\alpha$  of the low curvature part of the spectrum of the Hessian  $H$  for the skyrmion are shown in Fig. 2 (b-d). These modes have been discussed in several publications [17, 24, 34–36]. In Fig. 2 (b) the first of the two degenerated translations of the skyrmion is shown. The fourfold mode, or elongation mode, is depicted in Fig. 2 (c). An excitation of the skyrmion along this mode yields an elliptical deformation. The breathing mode, or scaling mode, changes the size of the skyrmion (See Fig. 2 (c)). These modes form the so called low curvature localized mode spectrum of the skyrmion in the lattice. Beyond these modes various boundary excitations populate the low eigenvalue spectrum.

For the application of the TRUMM method, we first use iterative displacements along certain eigenvectors to generate the starting points outside the convex region as in Ref. [17]. For each SP to be determined with the TRUMM method, we use six slightly different start configurations  $(\mathcal{I}_1, \dots, \mathcal{I}_6)$  which differ in how far they are outside the convex region of the local minimum of the skyrmion.

Briefly summarised, there is a relationship between iterative displacements along the eigenvector of the translation mode (breathing mode) for the generation of the starting points and the boundary SP (radial SP) through a subsequent application of the TRUMM methodology. The generation of the starting points for the duplication SP and the collapse of the skyrmion bag is more complex. See App. C for details.

For each of these start configurations, 50 computations were performed for both the TRUMM/RQM and the TRUMM/KS method, recording the mean of the

computation times  $t$  and the iterations  $k$  of the TRUMM method. Additionally, it was ensured that the calculation always terminated after the same number of iterations, as is to be expected for a deterministic algorithm. All calculations were performed on AMD Epyc 7313 processors with 32 cores (3.0 GHz). To compare the two algorithms, we computed the quotient of the walltimes  $\tau = t_{\text{RQM}}/t_{\text{KS}}$  and the number of needed iterations  $\kappa = k_{\text{RQM}}/k_{\text{KS}}$  (See Tab. II).

An example calculation of the duplication saddle point  $\text{Sp}_{\text{dup}}$ , initialized at  $\mathcal{I}_1$ , is shown for the TRUMM/RQM and TRUMM/KS method in Fig. 3 (d). One can identify slight quantitative differences between the two lowest eigenvalues, depending on which eigensolver (RQM or KS) is used within the TRUMM method.

This means that small differences in the determined eigenvectors accumulate to slightly different optimization paths of the method on the energy surface. Nevertheless, both methods converge reliably to the duplication SP, which is also true for the other five start configuration  $\mathcal{I}_2 - \mathcal{I}_6$ . The computation times and the number of iterations are depicted in Fig. 3 (b,c).

When comparing the average calculation times  $t_{\text{RQM}}$  ( $t_{\text{KS}}$ ) of the TRUMM/RQM (TRUMM/KS) and the iterations  $k_{\text{RQM}}$  ( $k_{\text{KS}}$ ) shown in Tab. II it is noticeable that a calculation using the RQM eigensolver is faster by a factor of 10 in this case, although a slightly longer path is followed on the energy surface resulting in a minor increase of the number of iterations. It is important to note that the RQM method only requires information about the first derivatives while the KS method, as implemented, also requires information about the Hessian matrix itself.

The results concerning the SP towards the skyrmion bag  $\text{Sp}_{\text{bag}}$  are shown in Fig. 4. Considering the first starting point for the TRUMM algorithm ( $\mathcal{I}_1$ ) the initial configuration has two negative eigenvalues with values close to each other. The application of the TRUMM algorithm (See Fig. 4 (d)) shows that both eigenvalues decrease before they increase again. This leads to a situation where the lowest eigenvalue is slightly negative and the second lowest eigenvalue is positive; thus the configuration constitutes a first order SP. It is noteworthy that such a situation requires the eigensolver to deliver a clear distinction between the eigenvectors of the lowest and second lowest eigenvalue while they are close to being degenerate. The RQM method is able to make this distinction for all tested situations.

As introduced in Sec. IID, the SPs identified with the TRUMM methodology can be used to generate meaningful initial paths for the application of the GNEB method. Fig. 5 shows the MEPs for the four discussed SPs, corresponding to the four investigated transitions of a skyrmion in this model. For the selected parameters of the Hamiltonian, the energy of the ferromagnetic state is higher than the energy of the isolated Skyrmion, and the local energy minimum of two Skyrmions in the lattice is the lowest. This suggests that the global minimum is a

skyrmion lattice.

## B. (Co-)Existence of Saddle Points

We shall now scan the parameter space, while keeping the exchange parameter  $J_1$  constant, and determine the ranges of existence of the four different SPs.

The computational efficiency of the implemented TRUMM/RQM method makes it feasible to perform such a scan, which is analogous to scanning the parameter space for meta-stability using local energy minimization calculations.

As discussed in Sec. IV A the identified SPs connect four distinct local energy minimum configurations: the isolated skyrmion (Skyr), two skyrmions (2 Skyr), the ferromagnetic state (FM) and the skyrmion bag (Bag), also called skyrmionium. First the meta-stability of these configurations is examined.

For that purpose, local energy minimizations, using a state to art LBFGS-method [37], are performed for magnetic fields strengths and DMI parameters in the parameter space defined in Tab. I. Those were initialized for each parameter point with all of the four aforementioned configurations obtained from the calculations in Sec. IV A at  $B = 3.1 \text{ T}$  and  $D = 0.55 \text{ meV}$ . The final configurations were then associated with one of the four states. The corresponding parameter regions of meta-stability are depicted in Fig. 6 (a). Note that only regions of meta-stability of all four states are shown, instead of depicting the corresponding lowest energy state and, thus, Fig. 6 (a) does not represent a phase-diagram.

For small magnetic fields at high DMI strength, the spin-spiral phase, which is not further considered here, is present. This parameter region is bounded by the meta-stability region of the ferromagnetic state. The largest parameter region of meta-stability for an isolated topological spin state within the ferromagnetic region is covered by the isolated Skyrmion. It is limited by the boundary of the ferromagnetic region to the spin-spiral phase and by the region of low DMI at high external magnetic fields. The latter boundary shares this region with the region of meta-stability of two Skyrmions in the lattice. However, an isolated skyrmion can exist at higher DMI strengths than two separated skyrmions. The meta-stability region of Skyrmion Bags covers only a narrow area located with comparatively high values of the DMI strength. The overlap with the two skyrmion region, therefore, is low. This overlapping area, in which all four local energy minima exist, is the region in which all four transition mechanisms  $\text{Sp}_{\text{rad}}$ ,  $\text{Sp}_{\text{bound}}$ ,  $\text{Sp}_{\text{dup}}$  and  $\text{Sp}_{\text{bag}}$  are expected to exist.

Subsequently, these regions of metastability were examined with respect to the existence of the previously identified types of SPs. Fig. 6 (b) illustrates this, for example, for the radial symmetric collapse of the isolated Skyrmion via the radial symmetric SP  $\text{Sp}_{\text{rad}}$  into the ferromagnetic state. This mechanism is expected only in the

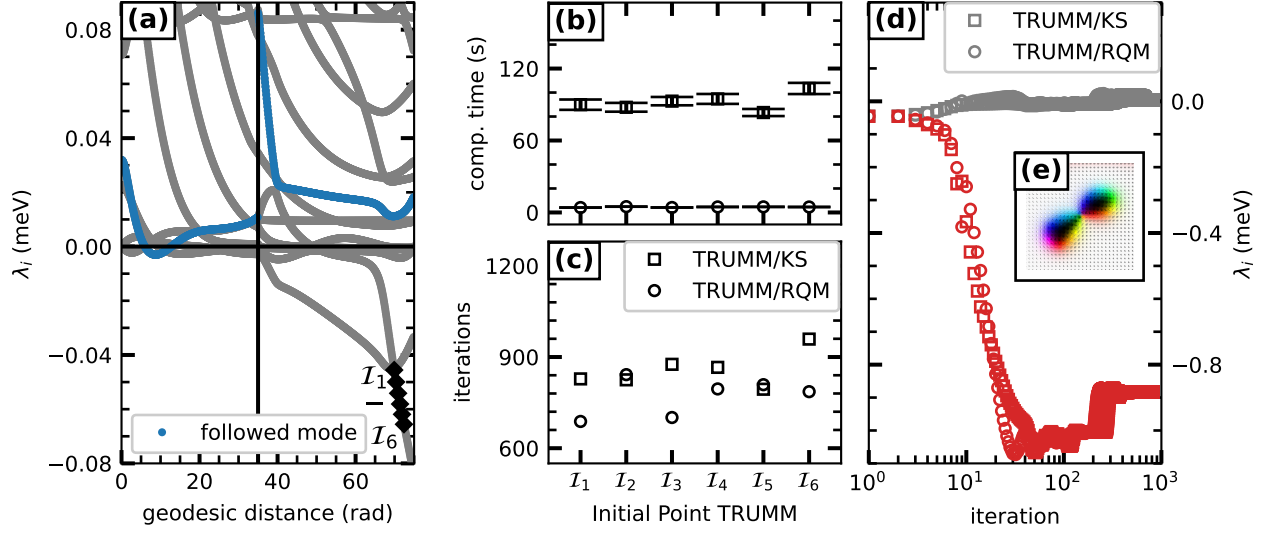


FIG. 3. (a): The left part represents the low curvature eigenvalue spectrum  $\lambda_\alpha$  during iterative displacements of the spin configuration along the eigenvector of the fourfold-mode starting from the skyrmion. The black line indicates the switching of the eigenvector for the iterative displacements to a mode higher in the spectrum ( $\alpha = 9$ ). Iterative displacements along this eigenvector are visualized in the right part. The six start configurations  $I_1 - I_6$  for the TRUMM method are marked with black diamonds. (b,c): Mean and standard deviation of the computation time for 50 calculations and number of iterations for each of the applications of the TRUMM/RQM and the TRUMM/KS algorithm to to each of the six starting configurations. (d): Two lowest eigenvalues of the current configuration during the application of the TRUMM/RQM and TRUMM/KS method for the exemplary case of starting point  $I_1$ . The inset (e) shows the resulting duplication SP  $Sp_{dup}$ .

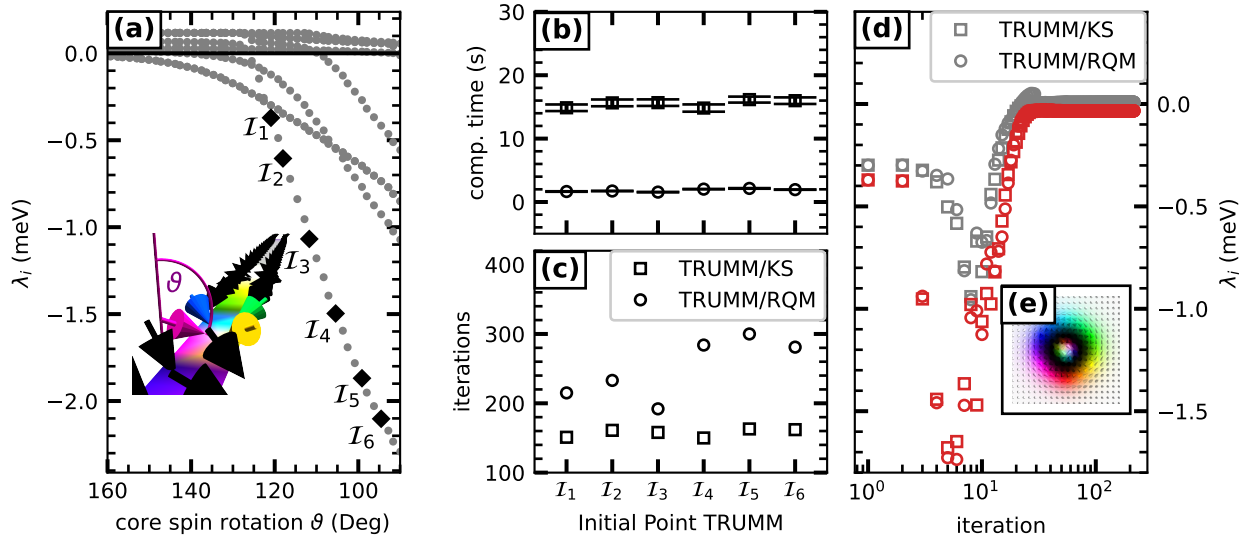


FIG. 4. (a): Low curvature eigenvalue spectrum for uniform rotation of the four core-spins of the skyrmion. The angle  $\theta$  gives the angle of the spins relative to the  $z$ -axis, while the in-plane component of the spins always points towards the center of the skyrmion. The leftmost point corresponds to the minimized skyrmion. The starting points for the TRUMM algorithm are indicated by the black diamonds. (b,c): Mean and standard deviation of the computation time for 50 calculations and number of iterations for each of the applications of the TRUMM/RQM and the TRUMM/KS algorithm to to each of the six starting configurations. (d): Two lowest eigenvalues of the current configuration during the application of the TRUMM/RQM and TRUMM/KS method for the exemplary case of starting point  $I_1$ . The inset (e) shows the resulting duplication SP  $Sp_{bag}$ .



TABLE II. Computational effort comparison for the Rayleigh Quotient Optimization (RQM) with the Krylov-Schur Method (KS) within the application of the TRUMM method to SPs of a Skyrmion, including the radial SP  $\text{SP}_{\text{rad}}$  and the boundary escape  $\text{SP}_{\text{bound}}$ , connecting the Skyrmion to the Ferromagnetic State, the duplication SP  $\text{SP}_{\text{dup}}$ , as well as the SP which connects the Skyrmion with the Skyrmion Bag  $\text{SP}_{\text{bag}}$ . For the latter two cases the initial points  $\mathcal{I}_1 - \mathcal{I}_6$  used with the TRUMM Method can be identified in Figs. 3,4. The mean  $t$  of the computation times as well as the iterations  $k$  are compared via  $\tau = t_{\text{RQM}}/t_{\text{KS}}$  and  $\kappa = k_{\text{RQM}}/k_{\text{KS}}$ .

Initial Point	TRUMM $\text{SP}_{\text{rad}}$		TRUMM $\text{SP}_{\text{bound}}$		TRUMM $\text{SP}_{\text{dup}}$		TRUMM $\text{SP}_{\text{bag}}$	
	$\tau$	$\kappa$	$\tau$	$\kappa$	$\tau$	$\kappa$	$\tau$	$\kappa$
$\mathcal{I}_1$	$0.14 \pm 0.04$	1.18	$0.08 \pm 0.05$	1.50	$0.05 \pm 0.02$	0.83	$0.12 \pm 0.04$	1.73
$\mathcal{I}_2$	$0.14 \pm 0.04$	1.07	$0.10 \pm 0.05$	2.05	$0.06 \pm 0.03$	1.02	$0.13 \pm 0.04$	1.84
$\mathcal{I}_3$	$0.14 \pm 0.05$	1.10	$0.10 \pm 0.04$	1.93	$0.04 \pm 0.02$	0.80	$0.14 \pm 0.04$	1.89
$\mathcal{I}_4$	$0.14 \pm 0.05$	1.09	$0.11 \pm 0.04$	2.09	$0.05 \pm 0.03$	0.92	$0.10 \pm 0.04$	1.22
$\mathcal{I}_5$	$0.14 \pm 0.04$	1.14	$0.10 \pm 0.04$	1.97	$0.06 \pm 0.04$	1.02	$0.11 \pm 0.05$	1.45
$\mathcal{I}_6$	$0.13 \pm 0.05$	1.06	$0.06 \pm 0.04$	1.09	$0.04 \pm 0.03$	0.82	$0.11 \pm 0.04$	1.42

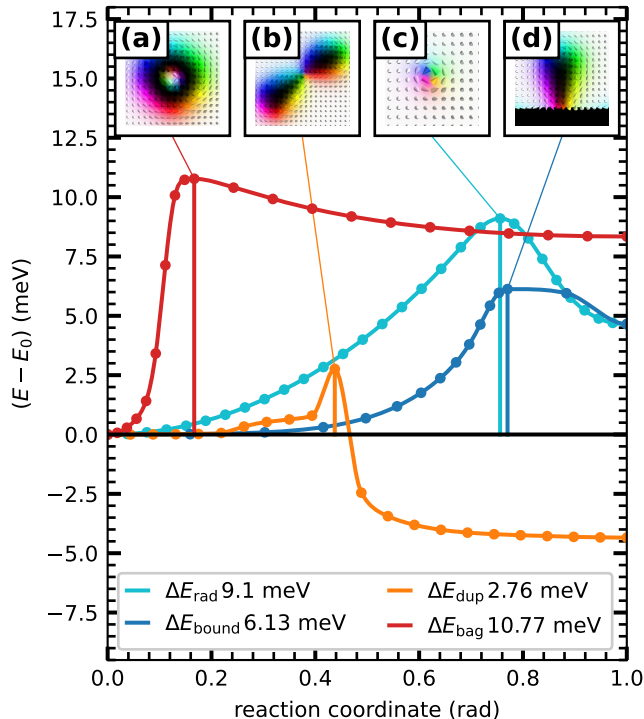


FIG. 5. Minimum Energy Paths (MEPs) obtained by ci-GNEB calculations [14] initialized with SPs obtained via the TRUMM algorithm. The insets show the first order SP configurations for the transition of the Skyrmion into the Skyrmion Bag (a), the duplication of an isolated Skyrmion, (b) the radial symmetric collapse (c) and the boundary collapse (d). The Energy Barriers are visualized by the vertical lines and their values are depicted in the legend.

region where the Skyrmion and the ferromagnetic state are meta-stable. Therefore, for each parameter point within this region, TRUMM/RQM calculations were initialized with the radial symmetric SP for  $B = 3.1$  T and  $D = 0.55$  meV determined in Sec. IV A.

Analogously, Fig. 6 (b), (c), (d) and (e) show the existence of the radial symmetric, the boundary, the duplication and the skyrmion bag collapse SP, respectively. The energy barrier for each collapse can be extracted by analysing the energy difference of the Skyrmion and the corresponding SP and is visualized by the displayed colormap.

In the same parameter region as for the radial symmetric SP, analogous calculations for the boundary collapse SP were performed (See Fig. 6 (c)). However, the corresponding existence region of this SP  $\text{Sp}_{\text{bound}}$  is smaller than for the radial symmetric SP. The calculations for the SP  $\text{Sp}_{\text{dup}}$  are limited to the overlap of meta-stability region of two Skyrmions and the parameter region of a single Skyrmion. This SP, therefore, occurs only for large DMI strengths in the regions of meta-stability of the associated minima. In the range of lower DMI strengths, we find that the transition, from an isolated

skyrmion to two separated skyrmions is, instead, mediated by a radial symmetric SP.

The existence region of the SP  $\text{Sp}_{\text{bag}}$ , which connects the isolated skyrmion to the skyrmion is the narrowest region among the observed mechanisms, since it is restricted to the meta-stability region of the skyrmion bag (See Fig. 6 (a)).

Fig. 6 (f) illustrates the dependence of the energy barriers  $\Delta E$  for each collapse type on the external magnetic field for a constant DMI value of  $D = 0.5$  meV. While the energy barriers for transitions to the ferromagnetic state decrease with increasing field strength, the energy barriers for the mechanisms leading to the transition to the state of two Skyrmions and the Skyrmion bag simultaneously increase. This is in line with expectations, as the amount of collinear spins of the target state decreases for the first two collapse types, starting from the minimum of the individual Skyrmion, while it increases for the latter two collapse types.

### C. First order saddle points in a 3D-System

The advantage of the finite difference RQM method, in terms of runtime and memory requirements, compared to using the explicit Hessian matrix, becomes particularly clear when systems with a large number of spins are analyzed. We, therefore, demonstrate the application of the TRUMM/RQM method to a cubic square lattice with  $30 \times 30 \times 30$  spins (see Tab. I for the parameters). Rybakov *et al.* performed GNEB calculations for this system and demonstrated the transition of a skyrmion tube (SkT) to the helical phase state, connected by two intermediate minima – two chiral bobbbers and a single chiral bobber (ChB) [33].

When investigating transition mechanisms of topological spin textures using the GNEB or CI-GNEB method, a critical task is the generation of an initial path. For example, the direct interpolation between initial and final state is often not sufficient for transitions involving translations of the spin texture. On the other hand, more complex initial paths require either physical intuition or prior knowledge of the system. We demonstrate that the TRUMM/RQM method is able to extract this crucial information, the energy barrier and the SP configurations, without prior knowledge of the system.

We initialize the system with random spin orientations (See Fig. 7 (b)). The many negative eigenvalues of the initial state grow during the process and strive towards positive values, as the configuration approaches the convex region around a local energy minimum. In each iteration of the TRUMM algorithm, the eigenmodes of the two lowest eigenvalues are determined using the RQM method. These are plotted in Fig. 7 (a). As can be seen from the corresponding inset, the eigenvalues of the lowest and second-lowest modes cross at some points, leading to a change of the lowest mode.

Summarily, we find two possible outcomes for such a

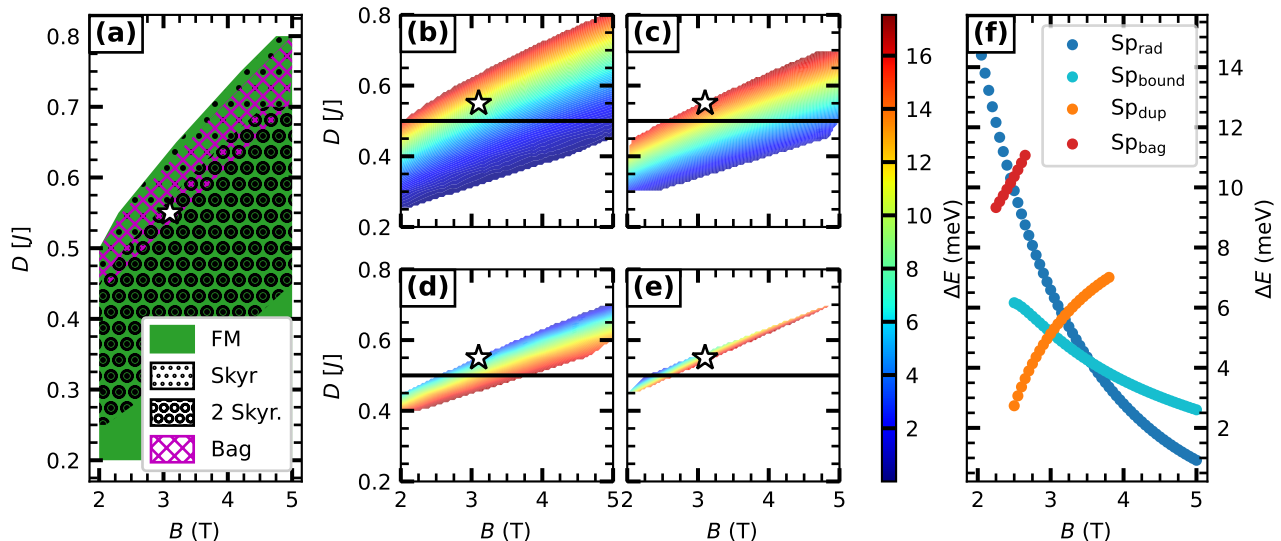


FIG. 6. (a): Meta-stability diagram concerning the meta-stability of the ferromagnetic state (FM), the isolated Skyrmion (Skyr.), two Skyrmions (2 Skyr.) and the Skyrmion Bag (Bag) obtained by energy minimization initiated with the corresponding states for the parameters  $B = 3.1$  T and  $D = 0.55$  meV (star symbol). (b-e): Existence diagrams for the SPs  $Sp_{\text{rad}}$ ,  $Sp_{\text{bound}}$ ,  $Sp_{\text{dup}}$  and  $Sp_{\text{bag}}$  obtained via the TRUMM/RQM method initialized with the corresponding SP at  $B = 3.1$  T and  $D = 0.55$  meV (star symbol). The colormap represents the corresponding energy barrier  $\Delta E$  regarding the energy of the Skyrmion state. (f): Exemplary behaviour of the energy barriers  $\Delta E$  for a constant DMI parameter of  $D = 0.55$  meV [horizontal lines in (b-e)] depending on the magnetic field for all the considered transitions.

minimization. Either, the method converges to a state with a single eigenvalue  $\lambda_1 < 0$  (See Fig. 7 (a)), called the unstable mode, or the process leads to a configuration within the convex region around a local minimum, as discussed in Sec. IID.

Fig. 7 (c) shows the resulting first order SP configuration. The meta-stable configurations of the adjacent energy minima are depicted in Fig. 7 (d,e). These configurations consist of combinations of well-known three-dimensional topological spin textures, such as Chiral Bobbers [33] or the so-called Globules [38]. The SP configuration found, depicted in Fig. 7, corresponds to the transition from a Globule to a Chiral Bobber.

The number of possible combinations of many such structures, in the simulation box, complicates a systematic investigation of various SP and energy minima configurations in this system. However, the presented calculation provides preliminary, yet important, insight into the cylindrical shape of topological spin textures in this system.

For the chosen parameters, we find ourselves in the helical phase [33], therefore, the TRUMM method is applied to another class of initial states. In the helical background, a cylinder with randomly oriented spins is considered (See Fig. 8 (a)). The application of the TRUMM method to 500 such random states resulted in the SP configurations shown in Fig. 8 (c). It is noteworthy that a series of additional SPs was found. These correspond to small energy barriers associated with lattice effects, such as translations. They are, however, not discussed

here. By identifying the respective neighboring minima, the schematic neighborhood diagram of local minima on the energy surface can be drawn, as shown in Fig. 8 (b). The transitions (i, iv, vi) correspond to the decay of a Skyrmion Tube (SkT) into the helical phase via intermediate states of two and one Chiral Bobber (ChB), as investigated with GNEB calculations in Ref. [33]. Müller *et al.* [38] point out that isolated Globules do not represent meta-stable configurations. However, it is possible to meta-stabilize them near Chiral Bobbers, as transitions ii and v show. To our knowledge, it is a new finding that the isolated globule state can represent a first-order SP in the helical phase (vii).

From the combination of the identified saddle-point configurations with minima discovered, the energy barriers  $\Delta E_{A \rightarrow B}$ , for a transition from a state  $A$  into some state  $B$ , can be obtained easily (See Tab. III). It should be noted that the state map, depicted in Fig. 8 (b), is likely not exhaustive. Interestingly however, many different states can be identified without relying on physical intuition. Additionally, meta-stable states with very small energy barriers, such as the combination of a single Globule with a Chiral Bobber, are present (See Tab. III).

## V. CONCLUSION

In this paper we presented the TRUMM method – an algorithm to efficiently identify first order SPs on an energy surface, given by a Hamiltonian with spin length

TABLE III. Energy barriers corresponding to the transitions and local energy minima configurations depicted in Fig. 8(b,c). Both energy barriers, the collapse of state A into state B with energy barrier  $\Delta E_{A \rightarrow B}$  as well as the transition of state B into state A with barrier  $\Delta E_{B \rightarrow A}$  are given.

State A \ State B	Energy barrier $\Delta E_{A \rightarrow B}$ (meV)					
	SkT	ChB	2 ChB	ChB + Globule	2 ChB + Globule	helical state
SkT	—	—	23.13	—	—	—
ChB	—	—	17.14	36.32	—	16.98
2 ChB	25.05	6.95	—	—	31.84	—
ChB + Globule	—	0.03	—	—	16.09	—
2 ChB + Globule	—	—	0.18	13.31	—	—
helical state	—	7.34	—	—	—	42.02

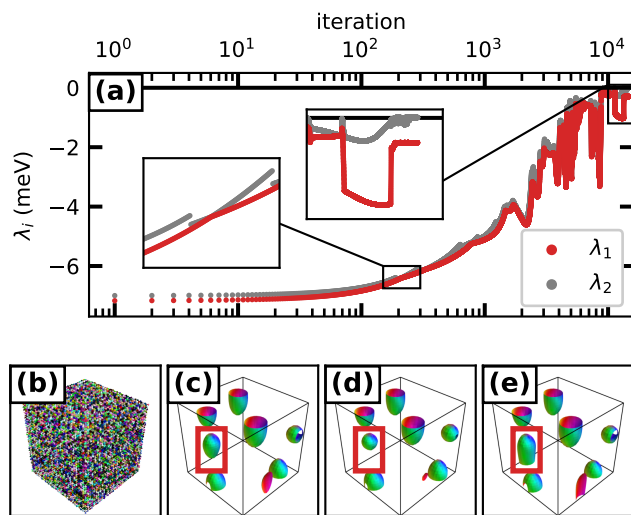


FIG. 7. Application of the TRUMM/RQM method to a cubic system with open boundaries in the  $z$ -direction initialized with a random spin configuration (b). (a): Representation of the two lowest eigenvalues  $\lambda_1, \lambda_2$  during the TRUMM/RQM algorithm. The insets highlight exemplary points of a mode crossing as well as the convergence to a state with a single negative eigenvalue  $\lambda_1$ . The configurations of the neighboring energy minima of the corresponding saddle-point configuration (c) are shown in parts (d) and (e). Here, the spin configuration is indicated by visualizing the isosurface of  $s_z = 0$  colored with the corresponding in-plane angle. A red outline in (e) indicates the transition from a Globule (d) to a Chiral Bobber (e).

constraints.

Further, we demonstrated a way of computing the eigenpairs, corresponding to the lowest eigenvalues of the Hessian matrix, making use of a direct optimization of the generalized Rayleigh quotient. The TRUMM/RQM method exploits the fast convergence of an initialised Rayleigh quotient and calculates the action of the Hessian matrix, using only information about the gradients. We found this strategy to be advantageous over previous implementations.

Employing the widely used atomistic Heisenberg

Hamiltonian, we have shown consistency with the results for skyrmions in a square lattice by Müller *et al.* [17].

The computational speed of the TRUMM/RQM makes the application to larger systems feasible. In particular, this enabled us to apply the method, for the first time, to a three-dimensional system, hosting chiral bobbers, skyrmion tubes and globules.

The stability of the developed method, with regard to the choice of starting points, was demonstrated within this three-dimensional system. We initialised the algorithm with random configurations, obtaining the same results, concerning the collapse of a skyrmion tube, that were by Rybakov *et al.* [33]. In contrast to previous approaches, no prior physical intuition was required. Furthermore, it was shown that the globule state, which cannot occur in isolation as a metastable state [38], can be a first-order SP in the helical phase. This information would not be accessible in mere energy minimisations.

On the one hand the method, developed here, complements existing methods for the calculation of transition reactions such as GNEB and its extensions. Usually, after finding a minimum energy path, with the GNEB method, an additional climbing image GNEB calculation is performed to determine the SP. The TRUMM/RQM method can replace this step by simply applying it to the highest energy image after the first GNEB calculation. Further, symbiotic effects between the GNEB methodology and the TRUMM method are possible, for example, in relation to the generation of initial paths by partial convergence of the TRUMM method. Summarily, we demonstrated an improved implementation of a method to discover SPs in magnetic systems, described by the Heisenberg Hamiltonian. The TRUMM method exhibits a high degree of computational efficiency and stability. These properties of the new implementation broaden the range of applicability of the method to more complex systems, exhibiting rich topology features.

## ACKNOWLEDGMENTS

M.S is grateful to A. Goswami and G. P. Müller for fruitful discussions. H.S is grateful to M. Görzen and S. Heinze for fruitful discussions. We gratefully ac-



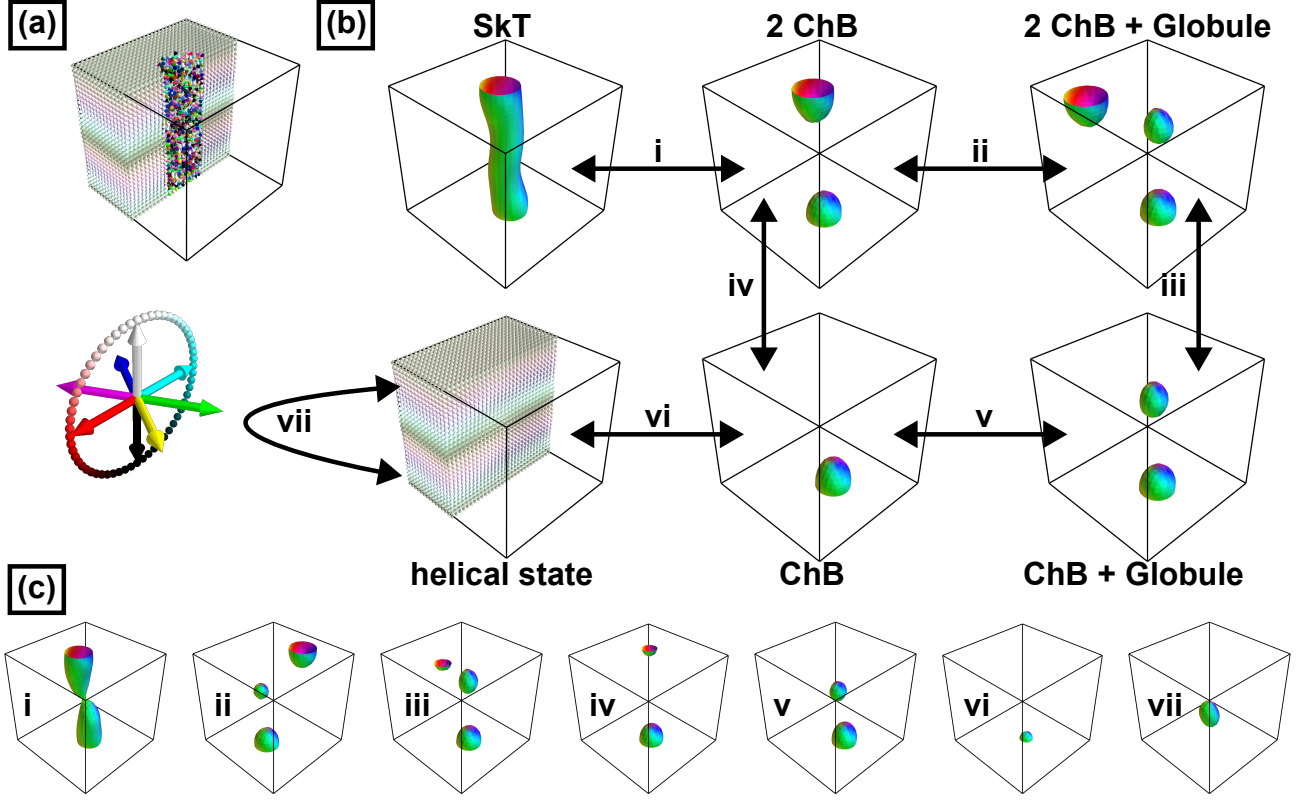


FIG. 8. Spin configuration corresponding to local energy minima (b) and first-order saddle points (c) obtained by the application of the TRUMM/RQM method initialized by states of a tube of random oriented spins in the background of the helical phase as depicted exemplarily in part (a). The iso-surface of each spin orientation  $s_z = 0.0$  is drawn and colored (See inset) by the respective in-plane angle of the spin orientation. (b): Visualization of the local energy minimum configurations Skyrmion Tube (SkT) and combinations of Chiral Bobbers (ChB) and Globules as well as the helical state. The arrows indicate transitions between the respective states and part (c) visualizes the corresponding first-order saddle point configurations.

knowledge financial support from the Icelandic Research Fund (Grants No. 239435 and No. 217750), the University of Iceland Research Fund (Grant No. 15673), the Swedish Research Council (Grant No. 2020-05110), and the Crafoord Foundation (Grant No. 20231063). This research was supported in part through high-performance computing resources available at the Kiel University Computing Centre.

M.S. and H.S. contributed equally to this work.

### Appendix A: Numerical Details

A key ingredient of the implemented TRUMM/RQM method is the implicit calculation of the action of the Hessian on an arbitrary vector. Here, we briefly summarize how to find the action

$$H\mathbf{x} = \mathbf{y} \quad (\text{A1})$$

of the  $2N$  Hessian matrix  $H \in \mathbb{R}^{2N \times 2N}$  on a vector  $\mathbf{x} \in \mathbb{R}^{2N}$  by applying a first order forward finite-difference scheme equipped with Richardson extrapolation. In order to avoid frequent base changes between the

local parametrizations of variables in the tangent space of the rotated and non-rotated spin configurations, the finite difference is calculated in the embedding euclidean  $3N$  space ( $\mathbf{x}^{3N} = U, \mathbf{x} \in \mathbb{R}^{3N}$ ). The spherical geometry of the spin configuration space will be considered by rotation of each spin  $s_i$  around an rotation axis  $\hat{k}_i = \vec{s}_i \times \frac{\vec{x}_i}{|\vec{x}_i|}$  by an angle  $\epsilon|\vec{x}_i|$ , where  $i$  indexes the component of the vector  $\mathbf{x}$  corresponding to the  $i$ -th spin. Such a rotation can be expressed by the matrix formulation of Rodriguez rotation formula:

$$R_{\epsilon, \mathbf{x}}^i = I + \sin(\epsilon|\vec{x}_i|)K^i + (1 - \cos(\epsilon|\vec{x}_i|))K^2 \quad (\text{A2})$$

with

$$K^i = \begin{pmatrix} 0 & -k_z^i & k_y^i \\ k_z^i & 0 & -k_x^i \\ -k_y^i & k_x^i & 0 \end{pmatrix}. \quad (\text{A3})$$

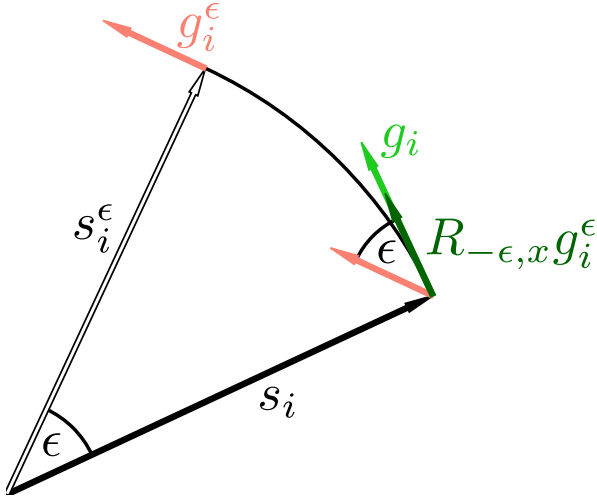


FIG. 9. Illustration of the quantities involved in calculating the action of the Hessian via forward finite differences with a steplength  $\epsilon$ .

The rotation matrix  $\mathcal{R}_{\epsilon,x}$  for the whole system is given by the direct sum of the individual rotation matrices:

$$\mathcal{R}_{\epsilon,x} = \bigoplus_{i=1}^N R_{\epsilon,x}^i = \begin{pmatrix} R_{\epsilon,x}^1 & 0 & \dots & 0 \\ 0 & R_{\epsilon,x}^2 & \dots & 0 \\ \vdots & \vdots & \ddots & \vdots \\ 0 & 0 & \dots & R_{\epsilon,x}^N \end{pmatrix}. \quad (\text{A4})$$

Now consider the Taylor expansion of the gradient  $\nabla E^\perp \in \mathbb{R}^{3N}$  projected to the tangent space of the current spin configuration  $\mathbf{S} \in \mathbb{R}^{3N}$  around this spin configuration with respect to change in the direction of  $\mathbf{x}$ :

$$\mathcal{R}_{-\epsilon,\mathbf{x}} \nabla E^\perp(\mathcal{R}_{\epsilon,\mathbf{x}} \mathbf{S}) = \nabla E^\perp(\mathbf{S}) + \epsilon U H \mathbf{x} + \mathcal{O}(\epsilon^2) \quad (\text{A5})$$

The gradient of the rotated spin configuration is rotated backwards to the tangent frame of the original spin configuration in order to compare all quantities in the same tangent space. This yields the following first-order forward finite difference scheme for the action of the constrained Hessian:

$$\mathbf{y} \approx U^T \frac{\mathcal{R}_{-\epsilon,\mathbf{x}} \nabla E^\perp(\mathcal{R}_{\epsilon,\mathbf{x}} \mathbf{S}) - \nabla E^\perp(\mathbf{S})}{\epsilon} \quad (\text{A6})$$

When considering the action for individual spins, the expression can be simplified to

$$\vec{y}_i = U_i^T \frac{[\vec{s}_i \cdot \vec{s}_i^\epsilon] \vec{g}_i^\epsilon + [\vec{g}_i^\epsilon \cdot \vec{s}_i^\epsilon] \vec{s}_i^\epsilon - \vec{g}_i}{\epsilon}, \quad (\text{A7})$$

where  $\vec{s}_i^\epsilon = \mathcal{R}_{\epsilon,x} \vec{s}_i$ ,  $\vec{g}_i^\epsilon = \vec{\nabla}_i E^\perp(S^\epsilon)$ ,  $\vec{g}_i = \vec{\nabla}_i E^\perp(S)$ . These quantities are illustrated in Fig. 9

The initial choice for the finite difference step size is always set to  $\epsilon = 10^{-6}$  while the maximum allowed error during Richardson extrapolation is defined as  $10^{-8}$ . The LBFGS based TRUMM algorithm is used without

a line search procedure. As described in Ref. [37] we restrict the maximum steplength with a parameter  $\vartheta_{\max}$ . The number of memory quantities taken into account is  $m = 3$  for all calculations in this publication. For the TRUMM calculations presented in Sec. IV A we always chose  $\vartheta_{\max}^{\text{TRUMM}} = 0.5$ . A TRUMM calculation is considered converged if the maximum force component drops below a value of  $10^{-12}$  eV/rad. Also the LBFGS solver of the RQM method was set to  $\vartheta_{\max}^{\text{RQM}} = 0.5$ . The calculation of the two lowest modes within the RQM method is considered converged if the norm of the Rayleigh Gradient on the Grassmannian drops below  $10^{-8}$ .

The KS eigensolver implemented in the extended eigensolver interface within the intel mkl library considers the extremal eigenpairs  $(\lambda_\alpha, \mathbf{v}_\alpha)$  as converged if

$$\frac{|H \mathbf{v}_\alpha - \lambda_\alpha \mathbf{v}_\alpha|}{|\lambda_\alpha|} \leq 10^{-5}, \quad (\text{A8})$$

where  $\mathbf{v}_\alpha$  is the representation of an eigenvector in  $2N$  tangent space basis.

## Appendix B: Pseudocode for optimization on the Grassmann manifold

As described in Sec. II, applying the L-BFGS optimizer to the Grassmann manifold requires some care. Here, we give a detailed pseudo code listing of what constitutes the "inner" L-BFGS solver, which computes the minimum modes. The main routine is given in Alg. 1. To compute the approximation of the action of the inverse Hessian, we use the well known "two loop recursion", listed in Alg. 2.

Clearly, Alg. 1, in combination with Alg. 2, constitutes a fairly standard L-BFGS method with some exceptions: A minor one is that the algorithm is being applied to matrices instead of – as perhaps more commonly seen – vectors. The other, much more important, exceptions is the use of the `Transport` and `Displace` function to move across the Grassmann manifold, in a way that respects its inherent geometry.

These two are implemented in Alg. 3 and Alg. 4, respectively, and make use of equations given by Edelmann *et. al.* [23].

## Appendix C: Escape Stage Details

A detailed investigation of the most efficient method for generating starting points for the TRUMM method outside the convex region of the meta stable state is beyond the scope of this paper. We describe here in detail how the start configurations for the TRUMM applications shown in Sec. IV A were obtained. Escaping the convex region for the radial SP  $\text{Sp}_{\text{rad}}$  and the boundary SP  $\text{Sp}_{\text{bound}}$  is achieved by iterative eigenvector displacements as shown in Fig. 10. Starting from

---

**Algorithm 1** L-BFGS optimizer for the generalized Rayleigh Quotient

---

**Require:** Initial point  $X$  on the Grassmann manifold  $G_{2,2N}$ , Hessian matrix  $H$ , tolerance  $\epsilon$ , maximum memory  $m$

**Ensure:** Solution  $X$  that spans the minimal invariant subspace of  $H$

Initialize  $k \leftarrow 0$

Initialize the history  $S \leftarrow [], Y \leftarrow [], \rho \leftarrow []$

**while**  $k < \text{maxIterations}$  **do**

// Here, we denote the action of the Hessian as  $HX$

// In practice, we use the finite difference scheme, described in App. A

$G_k \leftarrow 2X_k [HX_k - X_k(X_k^T HX_k)]$

**if**  $\|G_k\|_F < \epsilon$  **then**

**break**

**end if**

// Transport the history to the current tangent frame

**if**  $\text{len}(S) > 0$  **then**

$S_i \leftarrow \text{Transport}(X_{k-1}, S_i, U, \Sigma, V) \quad \forall S_i \in S$

$Y_i \leftarrow \text{Transport}(X_{k-1}, Y_i, U, \Sigma, V) \quad \forall Y_i \in Y$

**end if**

**if**  $k > 1$  **then**

// Append to the history

Append  $Q$  to  $S$

Append  $G_k - \text{Transport}(G_{k-1}, U, \Sigma, V)$  to  $Y$

Append  $\text{tr}[(X_k - X_{k-1})^T (G_k - G_{k-1})]^{-1}$  to  $\rho$

**if**  $\text{len}(S) > m$  **then**

Delete oldest entry of  $S, Y$  and  $\rho$

**end if**

// Curvature rejection condition

**if**  $\rho_{-1} < 0$  **then**

// Reset the history

$S \leftarrow [], Y \leftarrow [], \rho \leftarrow []$

**end if**

**end if**

// Compute the search direction via two loop recursion

$Q \leftarrow \text{TwoLoopRecursion}(S, Y, \rho, G_k)$

// Perform compact singular value decomposition of  $Q$  such that  $Q = U\Sigma V^T$

$U, \Sigma, V \leftarrow \text{SVD}(Q)$

// Update  $X$  via parallel transport

$X \leftarrow \text{Displace}(X, U, \Sigma, V)$

$k \leftarrow k + 1$

**end while**

---

the skyrmion, the configuration was displaced along the eigenvector of the breathing mode (Fig. 10 (a)) (translation mode (Fig. 10 (b))). This causes the skyrmion to shrink or move towards the open edge of the system. At a certain point, the lowest eigenvalue of the Hessian matrix becomes negative, indicating that the convex region around the initial minimum has been escaped. Six configurations  $\mathcal{I}_1$  to  $\mathcal{I}_6$  were then defined in the range of a negative lowest eigenvalue, which were used as starting points for the calculations of the TRUMM method (See Tab. II).

Generating suitable starting points for identifying the duplication  $\text{SP Sp}_{\text{dup}}$  is somewhat more complex than in

---

**Algorithm 2** Two loop recursion

---

**function**  $\text{TwoLoopRecursion}(S, Y, \rho, G)$

$Q \leftarrow G$

**for**  $i = \text{len}(S)$  **downto** 1 **do**

$\alpha_i \leftarrow \rho_i \text{tr}(S_i^T Q)$

$Q \leftarrow Q - \alpha_i Y_i$

**end for**

**if**  $\text{len}(S) > 0$  **then**

// Initial diagonal approximation

// for the inverse Hessian

$H_0^k \leftarrow \rho_i^{-1} \sqrt{\text{tr}(Y_k^T Y_k)}$

$Q \leftarrow H_0^k Q$

**end if**

**for**  $i = 1$  to  $\text{len}(S)$  **do**

$\beta \leftarrow \rho_i \text{tr}(Y_i^T Q)$

$Q \leftarrow Q + (\alpha_i - \beta) S_i$

**end for**

// Minus sign for minimization

**return**  $-Q$

**end function**

---



---

**Algorithm 3** Transport

---

**function**  $\text{Transport}(X, \Delta, U, \Sigma, V)$

// The parentheses are necessary to ensure a

// computationally efficient order of evaluation

$T_1 \leftarrow -XV \sin(\Sigma)(U^T \Delta)$

$T_2 \leftarrow U \cos(\Sigma)(U^T \Delta)$

$T_3 \leftarrow \Delta - U(U^T \Delta)$

**return**  $T_1 + T_2 + T_3$

**end function**

---

the two cases discussed so far. First, the skyrmion is iteratively displaced along the eigenvector of the four-fold mode. The corresponding low curvature eigenvalue spectrum is shown in the left part of Fig. 3 (a). The displacement along the eigenvector of this mode means an elongation of the skyrmion and none of the eigenmodes shows a rapid decrease of the associated eigenvalue during this process which would indicate suitable starting points for the TRUMM method. Indicated by the vertical black line in Fig. 3 (a), we change the eigenvector along which we displace to an eigenvector of the ninth smallest eigenvalue at this point. An iterative displacement (See Fig. 3 (a), right) causes the centre of the elongated skyrmion to narrow. This is accompanied in the eigenvalue spectrum by a rapid drop in an eigenvalue of a certain mode. In the region where this eigenvalue is the lowest in the spectrum, we again select six starting configurations  $\mathcal{I}_1 - \mathcal{I}_6$ . An application of the TRUMM algorithm leads to the duplication  $\text{SP Sp}_{\text{dup}}$  for all six configurations, although the configuration  $\mathcal{I}_1$  is chosen close to a mode crossing. If a configuration slightly left from this mode crossing is chosen, a TRUMM calculation leads back to the convex region of the skyrmion although

---

**Algorithm 4** Displace

---

```

function Displace( $X, U, \Sigma, V$ )
 $X_T \leftarrow XV \cos(\Sigma)V^T + U$ 
// Prevent accumulation of numerical errors
Orthonormalize columns of  $X_T$  with QR algorithm
return  $X_T$ 
end function

```

---

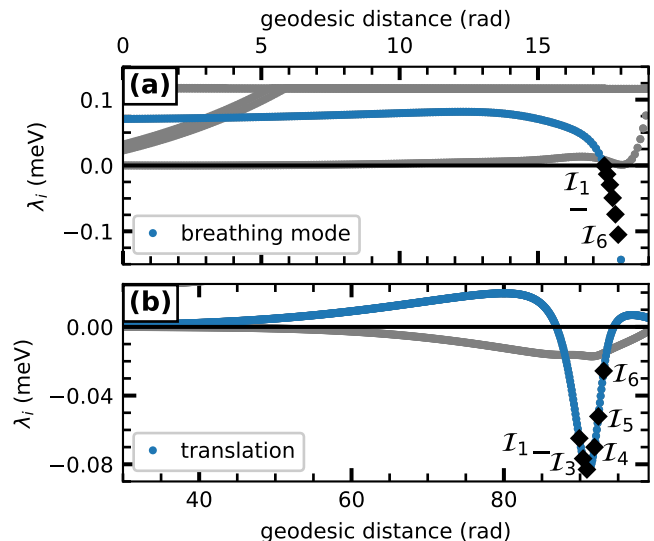


FIG. 10. Low curvature eigenvalue spectrum  $\lambda_i$  during iterative displacement along an eigenvector of the breathing mode (a) (translation mode (b)) starting from the skyrmion. The cumulated geodesic distance along this displacement is visualized on the  $x$ -axis. The eigenvalues of the minimum mode corresponding to six starting configuration  $\mathcal{I}_1$  to  $\mathcal{I}_6$  of the subsequent TRUMM application are marked with black diamonds.

the lowest eigenvalue is clearly negative in the beginning. This means that being outside the convex region is not a sufficient condition for the region of convergence of the TRUMM algorithm.

With regard to the SP configuration  $\text{Sp}_{\text{bag}}$  of the transition of a skyrmion into a skyrmion bag, no suitable starting points could be generated using the technique of iterative displacement along certain eigenvectors. Instead, the central four spins in the centre of the skyrmion are rotated in such a way that the in-plane component of each spin always points to the centre of the skyrmion while the out-of-plane angle is varied step by step. This is depicted schematically in the inset of Fig. 4 (a). The low curvature eigenvalue spectrum as well as the corresponding six starting configurations for the application of the TRUMM algorithm are visualized in Fig. 4 (a) for different out-of-plane angles  $\vartheta$ .

- 
- [1] E. Wigner, *Trans. Faraday Soc.* **34**, 29 (1938).
  - [2] G. H. Vineyard, *J. Phys. Chem. Solids* **3**, 121 (1957).
  - [3] H. A. Kramers, *Physica* **7**, 284 (1940).
  - [4] J. S. Langer, *Ann. Phys.* **54**, 258 (1969).
  - [5] G. Henkelman and H. Jónsson, *The Journal of Chemical Physics* **115**, 9657 (2001).
  - [6] H. Jónsson, *Proc. Natl. Acad. Sci.* **108**, 944 (2011).
  - [7] M. Plasencia Gutiérrez, C. Argáez, and H. Jónsson, *J. Chem. Theory Comput.* **13**, 125 (2017).
  - [8] D. Einarsdóttir, A. Arnaldsson, F. Óskarsson, and H. Jónsson, *Lect. Notes Comput. Sci.* **7134**, 45 (2012).
  - [9] V. Ásgeirsson, A. Arnaldsson, and H. Jónsson, *Lect. Notes Comput. Sci.* **148**, 102334 (2018).
  - [10] I. A. Nosikov, M. V. Klimenko, G. A. Zhibankov, A. V. Podlesnyi, V. A. Ivanova, and P. F. Bessarab, *IEEE Transactions on Antennas and Propagation* **68**, 455 (2020).
  - [11] B. Peters, *Reaction Rate Theory and Rare Events* (2017).



- p. 619.
- [12] W. Coffey, D. Garanin, and D. McCarthy, *Adv. Chem. Phys.* **117**, 483 (2001).
- [13] P. Bessarab, V. Uzdin, and H. Jonsson, *Phys. Rev. B* **85**, 10.1103/PhysRevB.85.184409 (2012).
- [14] P. F. Bessarab, V. M. Uzdin, and H. Jónsson, *Comput. Phys. Commun.* **196**, 335 (2015), arxiv:1502.05065.
- [15] A. V. Ivanov, D. Dagbartsson, J. Tranchida, V. M. Uzdin, and H. Jónsson, *J. Phys.: Condens. Matter* **32**, 345901 (2020).
- [16] V. Ásgeirsson, B. Birgisson, A., R. Bjornsson, U. Becker, F. Neese, and H. Jónsson, *J. Chem. Theory Comput.* **17**, 4929 (2021).
- [17] G. P. Müller, P. F. Bessarab, S. M. Vlasov, F. Lux, N. S. Kiselev, S. Blügel, V. M. Uzdin, and H. Jónsson, *Phys. Rev. Lett.* **121**, 197202 (2018).
- [18] G. P. Müller, H. Jonsson, C. Honerkamp, and S. Blügel, *Advanced Methods for Atomic Scale Spin Simulations and Application to Localized Magnetic States*, Ph.D. thesis, Dissertation, RWTH Aachen University, 2019. - Dissertation, University of Iceland, 2019 (2019).
- [19] M. Sallermann, H. Jónsson, and S. Blügel, *Phys. Rev. B* **107**, 104404 (2023).
- [20] K. Ohno and S. Maeda, *Chemical physics letters* **384**, 277 (2004).
- [21] S. Maeda, Y. Watanabe, and K. Ohno, *Chemical Physics Letters* **414**, 265 (2005).
- [22] G. W. Stewart, *SIAM J. Matrix Anal. Appl.* **23**, 601 (2002).
- [23] A. Edelman, T. Arias, and S. Smith, *SIAM Journal on Matrix Analysis and Applications* **20**, 10.1137/S0895479895290954 (1998).
- [24] A. S. Varentcova, S. von Malottki, M. N. Potkina, G. Kwiatkowski, S. Heinze, and P. F. Bessarab, *Npj Comput. Mater.* **6**, 193 (2020).
- [25] C. Lanczos, *J. RES. NATL. BUR. STAN.* **45**, 255 (1950).
- [26] E. R. Davidson, *Journal of Computational Physics* **17**, 87 (1975).
- [27] G. L. G. Sleijpen and H. A. Van der Vorst, *SIAM Rev.* **42**, 267 (2000).
- [28] D. C. Liu and J. Nocedal, *Mathematical Programming* **45**, 503 (1989).
- [29] B. Savas and L.-H. Lim, *SIAM J. Sci. Comput.* **32**, 3352 (2010).
- [30] N. Romming, C. Hanneken, M. Menzel, J. E. Bickel, B. Wolter, K. von Bergmann, A. Kubetzka, and R. Wiesendanger, *Science* **341**, 636 (2013).
- [31] F. Muckel, S. von Malottki, C. Holl, B. Pestka, M. Pratzner, P. F. Bessarab, S. Heinze, and M. Morgenstern, *Nat. Phys.* **17**, 395 (2021).
- [32] V. M. Kuchkin, B. Barton-Singer, F. N. Rybakov, S. Blügel, B. J. Schroers, and N. S. Kiselev, *Phys. Rev. B* **102**, 144422 (2020).
- [33] F. N. Rybakov, A. B. Borisov, S. Blügel, and N. S. Kiselev, *Phys. Rev. Lett.* **115**, 117201 (2015).
- [34] V. L. Zhang, C. G. Hou, K. Di, H. S. Lim, S. C. Ng, S. D. Pollard, H. Yang, and M. H. Kuok, *AIP Adv.* **7** (2017).
- [35] L. Desplat, D. Suess, J.-V. Kim, and R. L. Stamps, *Phys. Rev. B* **98**, 134407 (2018).
- [36] S. von Malottki, P. F. Bessarab, S. Haldar, A. Delin, and S. Heinze, *Phys. Rev. B* **99**, 060409 (2019).
- [37] A. V. Ivanov, V. M. Uzdin, and H. Jónsson, *Computer Physics Communications* **260**, 107749 (2021).
- [38] G. Müller, F. Rybakov, H. Jonsson, S. Blügel, and N. Kiselev, *Physical Review B* **101**, 10.1103/PhysRevB.101.184405 (2020).